Interplay of Device Design and Carbon-Doped GaN Buffer Parameters in Determining Dynamic R_{ON} in AlGaN/GaN HEMTs

Vipin Joshi, Sayak Dutta Gupta, *Graduate Student Member, IEEE*, Rajarshi Roy Chaudhuri, *Graduate Student Member, IEEE*, and Mayank Shrivastava, *Senior Member, IEEE*

***Abstract*— Using a well-calibrated computational framework, we reveal a complex interplay between the device design and the epi-stack parameters, which determines the electron trapping in the carbon-doped GaN buffer, leading to dynamic ON resistance (R_{ON}) in AlGaN/GaN HEMTs. The parameters being considered here are surface trap concentration, passivation thickness, field plate length, unintentionally doped (UID) GaN channel thickness, strain-induced piezoelectric polarization in the AlGaN layer, buffer traps, and carbon–Si co-doping of the GaN buffer. The role of surface traps in determining the extent of electron injection and trapping in the GaN buffer is revealed. Furthermore, its dependence on piezoelectric polarization in the AlGaN layer and implications on dynamic R_{ON} is discussed. Correlation among the passivation thickness, the field plate length, and the UID channel thickness affecting the channel electric field profile is explored, which, in turn, determines the extent of electron injection into the GaN buffer and eventually the extent of the dynamic R_{ON} degradation. This work also develops detailed physical insights explaining the mechanisms responsible for the disclosed complex interplay. This allowed us to discuss buffer-doping optimization to minimize electron trapping in the GaN buffer and resulting dynamic R_{ON} while maximizing the breakdown voltage of the device. These new findings are expected to provide guidelines to design dynamic R_{ON} resilient HEMTs and also to explain experimental trends associated with dynamic R_{ON} behavior as a function of the device and epi-stack parameters.**

***Index Terms*— AlGaN/GaN HEMTs, breakdown voltage, dynamic ON resistance, GaN buffer doping.**

Manuscript received 24 July 2022; revised 21 September 2022; accepted 21 September 2022. Date of publication 13 October 2022; date of current version 24 October 2022. This work was supported by the Department of Science and Technology (DST), Government of India, carried out at the Indian Institute of Science, Bengaluru, under Project SP/DSTO-21-0135. The work of Sayak Dutta Gupta and Rajarshi Roy Chaudhuri was supported by the DST INSPIRE Fellowship. The review of this article was arranged by Editor M. Meneghini. *(Corresponding author: Mayank Shrivastava.)*

The authors are with the Department of Electronic Systems Engineering, Indian Institute of Science, Bengaluru 560012, India (e-mail: mayank@iisc.ac.in; vipinjoshi@iisc.ac.in).

Color versions of one or more figures in this article are available at https://doi.org/10.1109/TED.2022.3209635.

Digital Object Identifier 10.1109/TED.2022.3209635

I. Introduction

TRAPPING in carbon-doped (C-doped) GaN buffer is known to introduce significantly dynamic ON resistance (dynamic R_{ON}) in AlGaN/GaN HEMTs [1], [2]. Given the high-voltage blocking capability offered by C-doping of GaN buffer, significant efforts have been made in the past to understand the mechanisms leading to dynamic R_{ON} and to mitigate this issue in AlGaN/GaN HEMTs [1], [2], [3], [4], [5], [6], [7], [8]. Surface and buffer optimization proposed in these works have improved dynamic R_{ON} performance to some extent. However, the physical mechanism governing the observed performance improvement is not well understood. A lack of understanding of the underlying physical mechanism limits the design space exploration and, hence, limits the device's performance. Moreover, novel processes associated with the trapping in the GaN buffer, such as the presence of a time-dependent critical drain stress voltage observed in the dynamic R_{ON} behavior of the device [2], require a comprehensive analysis of the impact of device design parameters on trapping in the GaN buffer and dynamic R_{ON} of the device.

Our recent works [9], [10] have established a complex interplay between surface and buffer parameters in determining the AlGaN/GaN HEMT device performance, which makes the design space exploration a non-trivial task. Impact of OFF-state electric field on dynamic R_{ON} has been discussed earlier in [11]. However, it does not discuss how device design parameters and their interplay can affect electric field conditions and the dynamic R_{ON} of the device. This establishes the requirement of a comprehensive analysis to determine the impact of device design parameters and their interplay in determining the dynamic R_{ON} behavior of the device.

Using a computational capability to accurately estimate dynamic R_{ON}, this work reports a physics-based analysis of the impact of device design and epi-stack parameters on electron trapping in the GaN buffer and, hence, dynamic R_{ON} of the device. Correlation between different design parameters in determining dynamic R_{ON} behavior of the device is analyzed to enable complete design space exploration for reducing trapping in the GaN buffer and minimizing dynamic R_{ON} of the device. Furthermore, considering the impact of carbon–silicon

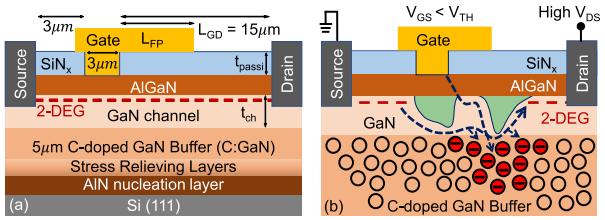

Fig. 1. (a) Schematic of the Schottky-gated AlGaN/GaN HEMT device on a C-doped GaN on Si power stack used in this work. (b) Schematic depicting the mechanism of electron trapping in the C-doped GaN buffer leading to dynamic R_{ON} in AlGaN/GaN HEMTs. The green region and blue arrows depict the potential depletion region and current leakage path, respectively.

co-doping of the GaN buffer on breakdown voltage (V_{BD}) of the device [12], its optimization with respect to V_{BD} as well as dynamic R_{ON} is discussed in correlation with other parameters. Such a device design analysis covering dynamic R_{ON} as well as breakdown voltage of the device is largely missing in the literature.

This article is organized as follows. Section II discusses the device structure and computational setup. Section III discusses the device design and GaN buffer parameters along with their correlation in determining dynamic R_{ON}. Physical insights into the observed dynamic R_{ON} behavior are also provided. Section IV discusses GaN buffer doping in correlation with device design parameters to optimize V_{BD} as well as dynamic R_{ON} of the device. Finally, Section V concludes the work.

II. Device Structure and Computational Setup

Fig. 1(a) shows the Schottky-gated AlGaN/GaN HEMT structure on a C-doped GaN-on-Si epi-stack used in this work. The device structure is similar to the one fabricated in our earlier works [2], [13] and showed excellent device characteristics with a V_{TH} of -0.8 V, an I_{ON} of 120 mA/mm at a V_{GS} of 2 V, and an I_{ON}/I_{OFF} ratio of 10^7 [2]. Moreover, a simulation setup is developed here for estimating the dynamic R_{ON} performance of the device and exhibited good agreement with the experimental data.

1) Carrier Transport and Dynamic R_{ON} Estimation: Carrier transport was modeled using drift–diffusion along with trap-assisted transport (TAT) for capturing carrier injection into the C-doped GaN buffer. A self-compensating trap profile was considered within the C-doped GaN buffer with the Poole Frenkel model-based field-dependent cross sections for capturing TAT and trapping in the C-doped GaN buffer. A constant self-compensation ratio of C-doping-induced traps, with an acceptor trap concentration ($BT_{acceptor}$) of 10^{18} cm^{-3} and a donor trap concentration (BT_{donor}) of 3×10^{16} cm^{-3}, enabled us to achieve good estimate for dynamic R_{ON} behavior. Moreover, the OFF-state stressing of the device allowed us to neglect lattice and carrier heating. Furthermore, drain and source contacts were modeled as Schottky contacts with lower work function and highly doped region in the contact proximity for accurate contact modeling [14]. Schottky gate with tunneling at the gate contact and a surface trap concentration of 3×10^{13} cm^{-2} enabled us to capture gate leakage dynamics [14] properly. Polarization charge in the device was estimated as follows: $q_{pol} = act_{pol}.\nabla\overrightarrow{P}$, where act_{pol} is a parameter for estimating piezoelectric polarization component, and $\overrightarrow{P}$ is the polarization vector evaluated, as discussed in [14]. In this work, piezoelectric charge in the AlGaN layer ($\sigma_{piezo,AlGaN}$) is varied by changing $act_{pol,AlGaN}$ (within the AlGaN layer) to account for changes in the piezoelectric polarization in the AlGaN layer. Further details about the computational setup can be found in our earlier works [9], [14]. The dynamic R_{ON} was extracted by a measure-stress-measure cycle. Pristine R_{ON} ($R_{Pristine}$) was measured before stressing the device in the OFF state. During the stress cycle, drain was biased at $V_{DS\text{-}Stress}$ for 100 μs with $V_{GS} = V_{TH} - 2$ V [2]. R_{ON} was also measured immediately after the stress cycle ($R_{Post\text{-}Stress}$) to calculate dynamic R_{ON} as $(R_{Post\text{-}Stress} - R_{Pristine})/R_{Pristine} \times 100\%$. R_{ON} is measured by taking inverse slope of the output characteristics at a V_{DS} of 0.25 and 0.5 V with $V_{GS} = 1$ V. $V_{DS\text{-}Stress}$ is varied in subsequent cycles to obtain dynamic R_{ON} as a function of $V_{DS\text{-}Stress}$. An L_{GD} of 15 μm with an L_{FP} of 1 μm is assumed for device analysis, unless stated otherwise.

2) V_{BD} Estimation: Besides dynamic R_{ON} estimation, the simulations also evaluated OFF-state V_{BD} of the device. Chynoweth law, calibrated for AlGaN/GaN HEMTs [9], [15], was used for estimating OFF-state V_{BD} of the devices. Here, V_{BD} is defined as the OFF-state drain voltage where the drain current reaches 10 μA/mm [16]. Furthermore, the substrate terminal was grounded for all the analyses.

III. Impact of Channel Electric Field Modulation on Dynamic R_{ON} in AlGaN/GaN HEMTs: Correlation With Device Parameters

Dynamic R_{ON} due to ionization of C-doping-induced traps in the GaN buffer depends on two processes: 1) hole emission [1] and 2) electron trapping [2], [13]. The hole emission process is known to be thermally activated and depends on applied drain voltage, stress time, and device temperature [1]. On the other hand, electron trapping is discussed in our earlier work [2] and is summarized in Fig. 1(b). As shown in the figure, electrons injected into the GaN buffer, through source–drain or gate leakage, get trapped in the C-doped GaN buffer near the gate or FP edge. Electric field magnitude near the gate/FP edge determines the concentration of electrons getting trapped near these edges and, hence, determines the dynamic R_{ON} of the device. Device parameters affecting electric field distribution and their impact on hole emission and electron trapping are discussed in this section.

A. Surface Donor Trap Concentration (ST_{donor}) and Piezoelectric Polarization in the AlGaN Layer

1) Impact on Dynamic R_{ON}: Surface donor traps and piezoelectric polarization in the AlGaN layer are known to affect n_S, channel electric field, and V_{BD} of the device [9], [14]. $\sigma_{piezo,AlGaN}$ or $act_{pol,AlGaN}$ is determined by the strain buildup in the AlGaN layer during the growth process. On the other hand,

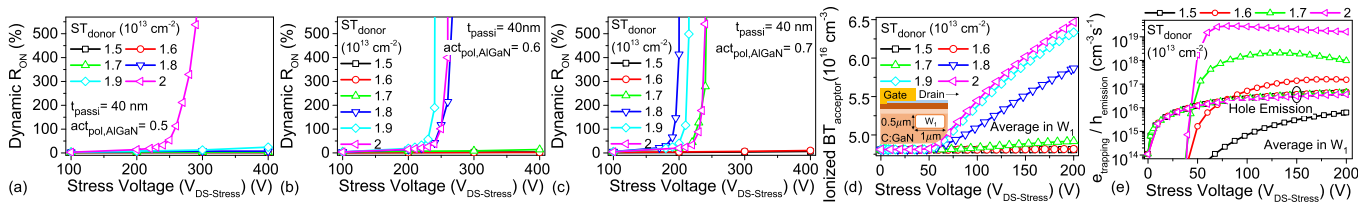

Fig. 2. Dynamic R_{ON} of the device extracted as a function of $V_{DS\text{-}Stress}$ for different surface donor trap concentrations and an $act_{pol,AlGaN}$ of (a) 0.5, (b) 0.6, and (c) 0.7. Average (d) ionized buffer acceptor trap concentration and (e) electron trapping and hole emission rate extracted in a window W_1 within the C-doped GaN buffer. The average values are extracted for a constant $act_{pol,AlGaN}$ of 0.6.

surface donor trap concentration can be effectively modulated by adopting a suitable surface passivation technique [9], [13]. Given that these parameters can modulate channel electric field conditions, their impact on the dynamic R_{ON} behavior of the device was evaluated. The parameters discussed here are chosen so as to have a minimum impact on V_{BD}, resulting in a fixed V_{BD} of ≈600 V. The impact of these parameters on V_{BD} of the device is discussed in detail in our previous works [9]. The impact of these parameters on dynamic R_{ON} of the device is shown in Fig. 2(a)–(c). The figures show the presence of a critical $V_{DS\text{-}Stress}$ (V_{cr}) beyond which dynamic R_{ON} of the device increases drastically, which is similar to V_{cr} observed experimentally in [2]. Fig. 2(a) further shows that as the surface donor trap concentration is reduced while maintaining a constant $act_{pol,AlGaN}$, the dynamic R_{ON} and V_{cr} of the device improve. On the other hand, as $act_{pol,AlGaN}$ is increased, Fig. 2(b) and (c) indicates that a lower ST_{donor} should now be achieved to improve the dynamic R_{ON} of the device. Furthermore, these figures indicate that the dynamic R_{ON} of the device again improves, as ST_{donor} is increased beyond a certain value. It should be noted that the surface traps can have a different impact on dynamic R_{ON} of the device, if it is stressed in the semi-ON state [17]. This is attributed to the presence of a high density of hot electrons in the semi-ON state, which can trigger trapping in the surface traps.

2) Underlying Physical Mechanism: Fig. 2(a)–(c) shows a significant dependence of dynamic R_{ON} and V_{cr} of the device on ST_{donor}, while a change in ST_{donor} is expected to modulate the absolute value of dynamic R_{ON} of the device; however, V_{cr} has a dependence on trapping in the GaN buffer [2]. Fig. 2(d) compares the average ionized $BT_{acceptor}$ as a function of ST_{donor}. It shows a significant reduction in ionized $BT_{acceptor}$, as ST_{donor} is reduced. This establishes ionized $BT_{acceptor}$ and ST_{donor} to be correlated. To understand this correlation, different sources of increase in ionized $BT_{acceptor}$, i.e., electron trapping and hole emission, are analyzed. Fig. 2(e) compares the electron trapping ($e_{trapping}$) and hole emission ($h_{emission}$) rates as a function of $V_{DS\text{-}Stress}$ for different values of ST_{donor}. The figure shows $h_{emission}$ to be independent of ST_{donor}. Furthermore, $h_{emission}$ does not exhibit any V_{cr}, such as stress voltage, beyond which it increases significantly. On the other hand, $e_{trapping}$ exhibits the V_{cr}-like phenomena and a ST_{donor} dependence, which is similar to that of ionized $BT_{acceptor}$, as seen in Fig. 2(d). This establishes $e_{trapping}$ to be responsible for observed dependence of dynamic R_{ON} on ST_{donor}. The increase in $e_{trapping}$ with ST_{donor} can be explained

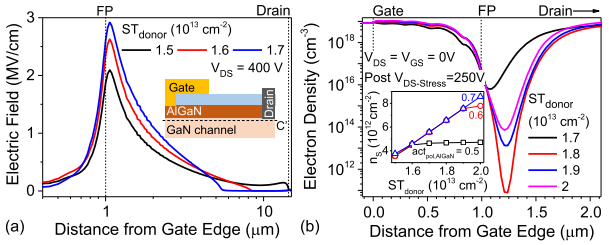

Fig. 3. (a) Lateral electric field extracted along a cutline C′ for different ST_{donor} values. (b) Channel electron density, extracted by bringing the device to initial stress condition post a 250-V stress cycle, for different values of ST_{donor}. $act_{pol,AlGaN}$ = 0.6 is considered here. Inset: 2-DEG density (n_s) as a function of ST_{donor} and $act_{pol,AlGaN}$.

by considering lateral channel electric field as a function of ST_{donor}, as shown in Fig. 3(a). It shows a relaxation in field peak near the FP edge, as ST_{donor} is reduced. A reduction in field peak near the FP edge reduces buffer trap ionization probability and, hence, improves the dynamic R_{ON} of the device, as ST_{donor} is reduced.

Fig. 2(b) and (c) further depicts an improvement in dynamic R_{ON} of the device, as ST_{donor} is increased beyond a certain value. However, the average ionized $BT_{acceptor}$ monotonically increases with an increase in ST_{donor}, as seen in Fig. 2(d). It should be noted here that, initially, the ionized $BT_{acceptor}$ increases significantly with ST_{donor}. However, the rate of increase reduces, as ST_{donor} is increased to higher values. On the other hand, the 2-DEG density (n_s) of the device increases with an increase in ST_{donor}, as seen in Fig. 3(b) (inset). This increase in n_s would, in turn, require a higher $BT_{acceptor}$ to result in a depletion similar to that of devices having a lower n_s or lower ST_{donor}. This is further evident from the channel electron density, extracted after bringing the device to rest condition ($V_{DS} = V_{GS} = 0$ V) immediately after a $V_{DS\text{-}Stress}$ of 250 V, shown in Fig. 3(b). The figure shows a reduced channel depletion for devices having an ST_{donor} of 2×10^{13} cm^{-2}, despite showing a higher $BT_{acceptor}$ [as seen in Fig. 2(d)]. Above discussion explains the observed dependence of dynamic R_{ON} of the device on ST_{donor}.

Fig. 2(a)–(c) also depicts a dependence of dynamic R_{ON} of the device on $act_{pol,AlGaN}$. For a given ST_{donor} value, the dynamic R_{ON} of the device degrades, as $act_{pol,AlGaN}$ is increased. This is attributed to an increase in ionized $BT_{acceptor}$, as $act_{pol,AlGaN}$ is increased, as shown in Fig. 4(a). While the ionized $BT_{acceptor}$ increased with $act_{pol,AlGaN}$, the electric

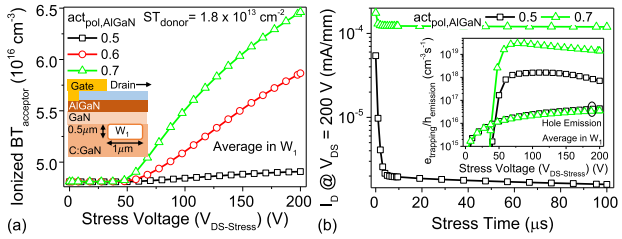

Fig. 4. (a) Average ionized buffer acceptor trap concentration, extracted in a window W_1, and (b) drain current as a function of $act_{pol,AlGaN}$. Inset: Average electron trapping and hole emission rate, both extracted in window W_1, for different values of $act_{pol,AlGaN}$.

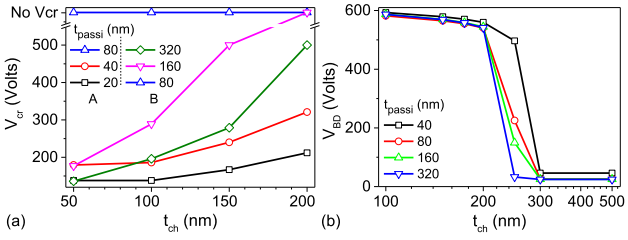

Fig. 5. (a) V_{cr} and (b) V_{BD} of the device as a function of t_{passi} and t_{ch}. V_{cr} is $V_{DS\text{-}Stress}$ for which dynamic R_{ON} becomes 100%. Variation in V_{cr} with t_{passi} is segregated in two regimes, A and B.

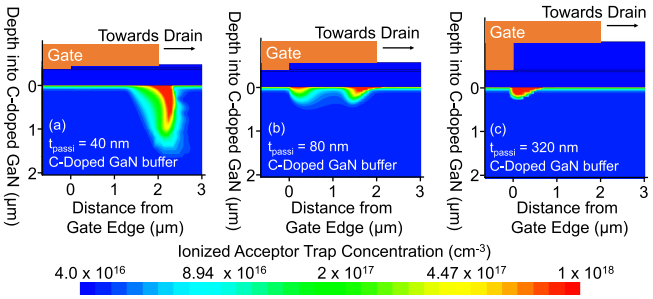

Fig. 6. Ionized $BT_{acceptor}$ extracted at a $V_{DS\text{-}Stress}$ of 300 V for a t_{passi} of (a) 40 nm (regime A), (b) 80 nm (regimes A and B), and (c) 320 nm (regime B).

field was found to be independent of $act_{pol,AlGaN}$ (data not shown here) for the considered range of $act_{pol,AlGaN}$ and ST_{donor}. On the other hand, Fig. 4(b) depicts an increase in the OFF-state drain current (I_D), as $act_{pol,AlGaN}$ is increased. Furthermore, this increase in I_D is accompanied by an increase in $e_{trapping}$, as shown in Fig. 4(b) (inset). At the same time, $h_{emission}$, also shown in Fig. 4(b) (inset), is found to be independent of $act_{pol,AlGaN}$. The higher dynamic R_{ON} for devices with higher value of $act_{pol,AlGaN}$ is, thus, caused by an increase in $e_{trapping}$, resulting from a higher leakage current in these devices. The increase in leakage current with $act_{pol,AlGaN}$ is attributed to an increase in the vertical polarization-induced electric field within the AlGaN layer [14], which increases the tunneling-induced gate leakage.

The above discussion establishes that the field relaxation achieved by a lower ST_{donor} can improve the dynamic R_{ON} of the device. This has also been demonstrated experimentally in our recent work [13]. To analyze the impact of other device parameters on dynamic R_{ON}, a higher ST_{donor} of 3×10^{13} cm^{-2} with $act_{pol,AlGaN} = 0.5$ is used in the subsequent sections. Accounting for device design optimization for higher ST_{donor} allows the analysis of the complete design space.

B. Passivation (t_{passi}) and UID GaN Channel (t_{ch}) Thickness

t_{passi} and t_{ch} can modulate channel electric field conditions and leakage current [12], respectively, and, thus, can affect dynamic R_{ON} of the device. Moreover, since t_{passi} also modulates the vertical field near the FP edge, it can also affect the leakage current path. This makes t_{passi} and t_{ch} to be dependent variables that should be considered simultaneously to determine the dynamic R_{ON} of the device.

1) Impact on Dynamic R_{ON}: Fig. 5(a) compares V_{cr} of the device as a function of t_{ch} and t_{passi}. Dependence of dynamic R_{ON} on t_{passi} can be categorized into two regimes A and B with $t_{passi} = 80$ nm as the boundary value. In regime A, dynamic R_{ON} of the device improves with increasing t_{passi}. Moreover, devices show an increased dependence on t_{ch}, as t_{passi} is increased. On the other hand, as t_{passi} is increased further, i.e., for devices in regime B, the dynamic R_{ON} of the device degrades with an increase in t_{passi}. Moreover, the dependence of dynamic R_{ON} on t_{ch} also reduces, as t_{passi} is increased. This difference in behavior as t_{passi} is varied in regimes A and B suggests different trapping mechanisms responsible for the observed dynamic R_{ON} characteristics.

On the other hand, V_{BD} of the device shows negligible variation with t_{passi}, as shown in Fig. 5(b). The t_{passi} independent V_{BD} indicates a vertical breakdown in these devices. It is worth highlighting here that though V_{BD} is independent of t_{passi}, dynamic R_{ON} of the device shows a dependence on it. Furthermore, V_{BD} reduces marginally, as t_{ch} is increased up to 200 nm. However, it reduces sharply, as t_{ch} is increased beyond 200 nm, thereby restricting the design window to $t_{ch} = 200$ nm for optimizing dynamic R_{ON} performance.

2) Underlying Physical Mechanism: As discussed in the previous section, the difference in the dynamic R_{ON} of devices as t_{passi} is varied in regimes A and B, suggesting the trapping process to be different in the two regimes. To understand these trapping processes, Fig. 6 compares ionized buffer acceptor trap profile for devices with different t_{passi} values and similar t_{ch} values. It depicts maximum trap ionization to be near the FP edge for devices with thinner t_{passi} (regime A) [see Fig. 6(a)]. With an increase in t_{passi} [see Fig. 6(b)], trap ionization reduces near the FP edge; however, trap ionization now also starts happening near the gate edge. As t_{passi} is increased further (regime B) [see Fig. 6(c)], the trap ionization near the FP edge completely disappears. However, now, the trap ionization near the gate edge increases in magnitude. This indicates a shift in trapping affected region from FP edge to gate edge, as t_{passi} is increased. This shift in trapping regime from FP edge to gate edge can, in turn, be explained by comparing the electric field profile for devices with different t_{passi} values, as shown in

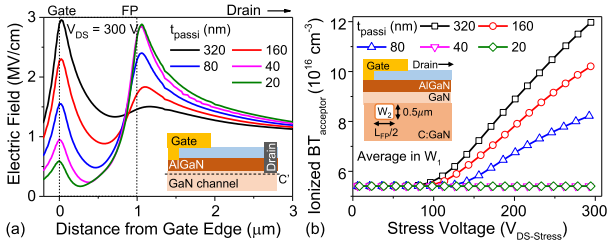

Fig. 7. (a) Lateral electric field in the channel region extracted along a cutline C′ as a function of t_{passi}. The field profile is extracted by reducing trapping in the GaN buffer to zero for a fair comparison. (b) Average ionized $BT_{acceptor}$ extracted for different t_{passi} values and a t_{ch} of 150 nm within a window W_2 in the GaN buffer.

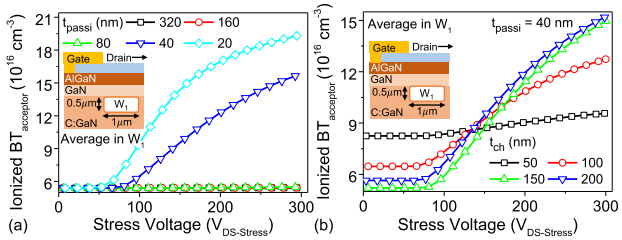

Fig. 8. Average ionized $BT_{acceptor}$ evaluated in a window W_1 near the field plate edge for (a) different t_{passi} values with a t_{ch} of 150 nm and (b) different t_{ch} values with a t_{passi} of 40 nm.

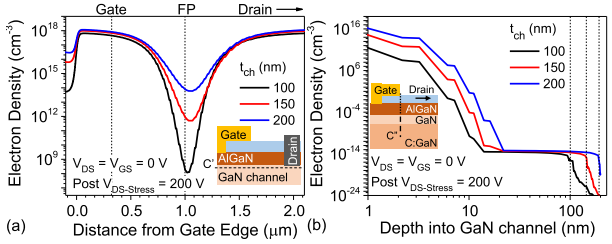

Fig. 9. Electron density extracted along (a) horizontal cutline C′ and (b) a vertical cutline C″ for different t_{ch} values. A t_{passi} of 40 nm is considered. For extracting the electron densities, the device was brought to rest condition after forcing it through a stress cycle with $V_{DS\text{-}Stress}$ = 200 V.

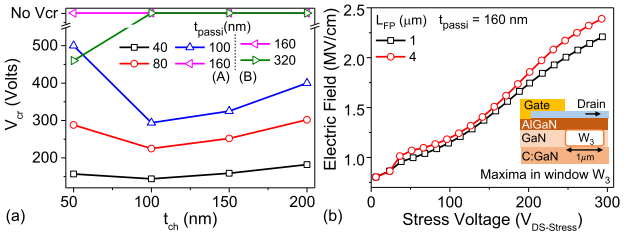

Fig. 10. (a) Critical $V_{DS\text{-}Stress}$ observed in dynamic R_{ON} characteristics of devices with L_{FP} = 4 μm. Variation in V_{cr} with t_{passi} is segregated in two regimes, A and B. (b) Peak magnitude of electric field in a window near the field plate edge as a function of $V_{DS\text{-}Stress}$ and L_{FP}.

Fig. 7(a). It shows a reduction in field magnitude near the FP edge and an increase in field magnitude near the gate edge, as t_{passi} is increased. This change in field magnitude explains the observed shift in the trapping regime in the GaN buffer.

To further understand the dependence of trapping on t_{passi}, the average of ionized $BT_{acceptor}$ is extracted in two windows W_2 and W_1, as shown in Figs. 7(b) and 8(a), respectively. While W_2 captures trapping near the gate edge, W_1 captures trapping near the FP edge. Fig. 7(b) indicates that the trapping near the gate edge increases, as t_{passi} is increased and becomes significant for $t_{passi} \geq 80$ nm. This leads to an increase in dynamic R_{ON}, as t_{passi} is increased in regime B. On the other hand, Fig. 8(a) indicates that the trapping near the FP edge increases, as t_{passi} is reduced. This explains the observed increase in dynamic R_{ON} with a reduction in t_{passi} for devices in regime A. This dependence of ionized $BT_{acceptor}$ on t_{passi} is similar to that of electric field dependence on t_{passi} [see Fig. 7(a)], thereby establishing electric field profile to be responsible for the observed behavior, As explained earlier, the electric field has a minimal impact on hole emission, but it significantly modulates electron trapping [see Figs. 2(e) and 4(b)]. This further establishes electron trapping to be responsible for the observed dynamic R_{ON} behavior of the device.

To understand the dependence of dynamic R_{ON} on t_{ch}, the average ionized $BT_{acceptor}$ was extracted for different t_{ch} values and is shown in Fig. 8(b). It shows that the average trapped charge decreases with a reduction in t_{ch}, and this should lead to a lower dynamic R_{ON} for devices with a thinner channel. However, thinner channel devices exhibited degraded dynamic R_{ON} behavior, as seen in Fig. 5(a). Despite having a lower trapped charge, the 2-DEG charge density extracted after the stress cycle shows an increased channel depletion near the FP edge for thinner channel devices, as shown in Fig. 9(a). This increase in channel depletion despite having lower trapped charge density for thinner channel devices can be explained by considering the t_{ch} thickness that is being depleted, as shown in Fig. 9(b). It shows that the devices with thinner channel need to deplete a smaller area to deplete the 2-DEG. This leads to enhanced channel depletion for thinner channel devices even with a lower ionized $BT_{acceptor}$.

The above discussion establishes 2-DEG charge depletion and, hence, the dynamic R_{ON} of the device to be dependent on the following: 1) t_{ch} and 2) magnitude of trapped charge in the C-doped GaN buffer. A higher trapped charge density will allow 2-DEG depletion even for devices with thicker channel, and hence, the devices with thicker channel also exhibit significantly dynamic R_{ON}. This is observed for devices with thinner t_{passi} in regime A [seen in Fig. 5(a)] and for devices with thicker t_{passi} in regime B [seen in Fig. 5(a)]. These devices showed a higher trapped charge density, as seen in Fig. 8(a) and (b) for devices in regimes A and B, respectively. This establishes requirement of considering t_{passi} and t_{ch} simultaneously while evaluating the dynamic R_{ON} of the device.

C. Field Plate Length

L_{FP} can modulate electric field conditions near the gate and field plate edge, which can directly modulate dynamic R_{ON} of the device. This makes L_{FP} an important design parameter.

1) Impact on Dynamic R_{ON}: Fig. 10(a) compares V_{cr} for devices having an L_{FP} = 4 μm for different values of

t_{passi} and t_{ch}. Devices show a similar dependence on t_{passi} as observed for $L_{FP} = 1$-μm devices [shown in Fig. 5(a)]. V_{cr} initially increases, as t_{passi} is increased with devices having a t_{passi} of 160 nm showing the best dynamic R_{ON} behavior. However, as t_{passi} is increased beyond 160 nm, the devices start showing a V_{cr} for thinner GaN channels. As discussed for devices with $L_{FP} = 1$ μm, the device behavior with t_{passi} can again be divided into two regimes A and B with $t_{passi} =$ 160 nm segregating these two regimes. It should be noted that t_{passi} determining the segregation between regimes A and B is higher for devices with $L_{FP} = 4$ μm ($\approx$160 nm) as compared to devices with $L_{FP} = 1$ μm ($\approx$80 nm). Moreover, the devices with a larger L_{FP} of 4 μm show a lower V_{cr} as compared to devices with $L_{FP} = 1$ μm [shown in Fig. 5(a)] except for devices with $t_{ch} = 50$ nm. As seen from Fig. 10(a), V_{cr} for devices with $t_{ch} = 50$ nm and $L_{FP} = 4$ μm is higher than or equal to that of devices with $t_{ch} > 50$ nm and $t_{passi} < 320$ nm. However, as t_{passi} is increased to 320 nm, the devices with a t_{ch} of 50 nm again start showing a lower V_{cr}. This is in contrast to devices with $L_{FP} = 1$ μm, wherein a t_{ch} of 50 nm always resulted in a V_{cr} lower than that of devices with thicker channel, irrespective of the t_{passi} value [see Fig. 5(a)].

It is worth highlighting here that L_{FP} of the device is expected to modulate V_{BD} as well. However, as discussed earlier, V_{BD} in these devices was determined by vertical stack breakdown and was independent of L_{FP} (data not shown here). It should be noted that improving the vertical voltage handling capability of the device would result in an L_{FP} dependence of V_{BD} and will be discussed in later sections. However, as the discussion so far and in this section correlates dynamic R_{ON} with the electric field, these findings remain valid even if V_{BD} is determined by lateral device breakdown.

2) Underlying Physical Mechanism: To gain further insights into the phenomenon responsible for the increase in dynamic R_{ON} with L_{FP}, the electric field magnitude near the field plate edge is compared for devices with different L_{FP} values. The results, as shown in Fig. 10(b), show a higher electric field magnitude near the FP edge for devices with larger L_{FP} for the same applied $V_{DS\text{-}Stress}$. Here, the devices with $t_{passi} =$ 160 nm and $t_{ch} = 150$ nm are considered for comparing field conditions, as these devices have very high V_{cr} ($\geq$500 V) [see Figs. 5(a) and 10(a)] with negligible trapping in the GaN buffer. This allows us to compare field conditions that are not modulated by trapping in the GaN buffer [10]. The observed higher electric field near the FP edge, for devices with larger L_{FP}, leads to the earlier onset and increases in the magnitude of trapping in the C-doped GaN buffer for larger L_{FP} devices, as shown in Fig. 11(a). This, in turn, leads to lower V_{cr} in devices having larger L_{FP}.

a) Explanation for dependence on t_{passi}: As devices with larger L_{FP} result in a higher field magnitude near the FP edge, a thicker t_{passi} is required for these devices to achieve a field magnitude similar to that of devices with shorter L_{FP}. Given that electric field conditions modulate electron trapping, which determines V_{cr}, thicker passivation is required to achieve improvement in dynamic R_{ON} in larger L_{FP} devices as compared to devices with shorter L_{FP}.

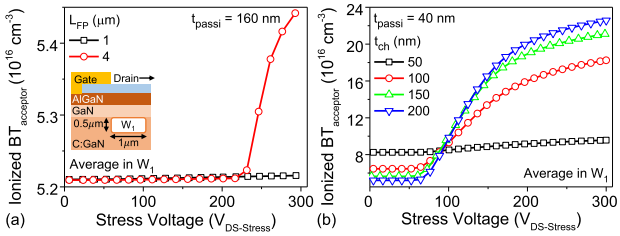

Fig. 11. (a) Average ionized $BT_{acceptor}$, evaluated in the window W_1, as a function of $V_{DS\text{-}Stress}$ for devices with different L_{FP} values. Devices had a t_{ch} of 150 nm. (b) Average ionized buffer acceptor trap density extracted for different t_{ch} values within the same window W_1 for a device with $L_{FP} = 4$ μm.

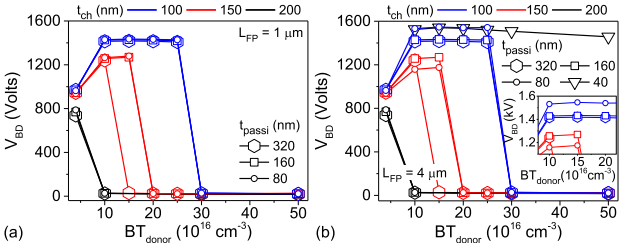

Fig. 12. V_{BD} as a function of BT_{donor} for devices with an L_{FP} of (a) 1 and (b) 4 μm. Inset: Optimized conditions that result in a V_{BD} improvement with L_{FP}. $BT_{acceptor}$ is taken as 10^{18} cm^{-3}.

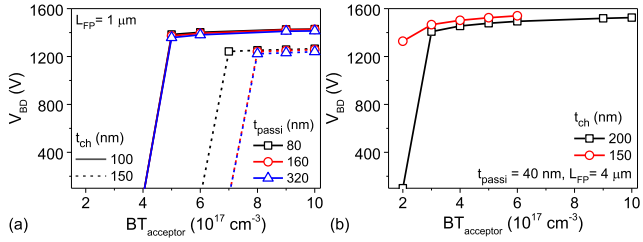

Fig. 13. V_{BD} of the device as a function of $BT_{acceptor}$ for a constant BT_{donor} of 10^{17} cm^{-3}. Devices have an L_{FP} of (a) 1 and (b) 4 μm.

b) Explanation for dependence on t_{ch}: As discussed in Section III-B2, the impact of t_{ch} on dynamic R_{ON} is determined by the following: 1) magnitude of the charge trapped in the C-doped GaN buffer and 2) channel thickness to be depleted by this charge. Fig. 11(b) compares the average trapped electron charge in a window near the FP edge for different t_{ch} values. A comparison of this trapped charge with that for devices with $L_{FP} = 1$ μm [see Fig. 8(b)] shows a similar dependence on t_{ch}. However, the average trapped charge is considerably higher for devices with larger L_{FP}. Given that the average trapped charge can be reduced by increasing t_{passi}, a thicker t_{passi} is now required to reduce this trapped charge to the levels equivalent to that for devices with $L_{FP} = 1$ μm. Moreover, as t_{ch} can modulate the 2-DEG depletion only if average trapped charge is sufficiently low, the longer L_{FP} devices show an improvement in dynamic R_{ON} with t_{ch} only after t_{passi} is increased beyond 80 nm.

The distinct behavior of devices with a t_{ch} of 50 nm is attributed to lower ionized $BT_{acceptor}$ in these devices, as seen in Fig. 11(b). A similar reduction in trapped charge

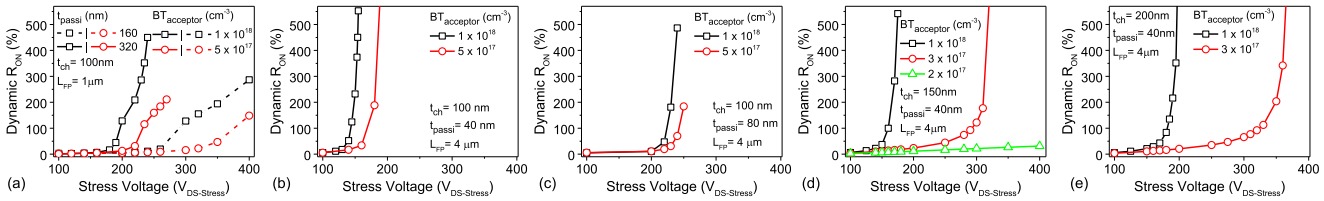

Fig. 14. Dynamic R_{ON} of the device extracted as a function of $V_{DS\text{-}Stress}$ for different optimized $BT_{acceptor}$ values. Different device structures are evaluated with (a) $L_{FP} = 1\ \mu m$, $t_{ch} = 100$ nm, and varying t_{passi}; (b) $L_{FP} = 4\ \mu m$, $t_{ch} = 100$ nm, and $t_{passi} = 40$ nm; (c) $L_{FP} = 4\ \mu m$, $t_{ch} = 100$ nm, and $t_{passi} = 80$ nm; (d) $L_{FP} = 4\ \mu m$, $t_{ch} = 150$ nm, and $t_{passi} = 40$ nm; and (e) $L_{FP} = 4\ \mu m$, $t_{ch} = 200$ nm, and $t_{passi} = 40$ nm. BT_{donor} is taken as 10^{17} cm^{-3}.

concentration was observed for devices with an L_{FP} of 1 μm. However, due to the thinner channel, the impact of this reduced trapping becomes evident only when the ionized trap concentration is sufficiently low to have a minimal impact on the 2-DEG charge density. Hence, the effect is visible only when $t_{passi} \geq 80$ nm for devices with $L_{FP} = 4\ \mu$m. The above discussion establishes that a larger L_{FP} mandates requirement of a thicker t_{passi} for optimizing dynamic R_{ON} of the device.

IV. Optimizing GaN Buffer Doping in Correlation With Device Parameters

Device design till now had focused on improving the dynamic R_{ON} of the device. Vertical stack breakdown resulted in negligible impact of these parameters on V_{BD} of the device. The voltage handling capability of the GaN buffer can be improved by independently optimizing $BT_{acceptor}$ and BT_{donor} [12]. The current section analyzes the impact of these parameters on the dynamic R_{ON} of the device and correlates it with the device parameters discussed till now. A higher ST_{donor} of 3×10^{13} cm^{-2} with $act_{pol,AlGaN} = 0.5$ is considered in this section, as devices with lower ST_{donor} had negligible dynamic R_{ON}.

A. Optimizing V_{BD} of the Device

1) Maximizing BT_{donor}: Fig. 12 shows the impact of increasing BT_{donor} on V_{BD} of the device for a given $BT_{acceptor}$. It indicates a considerable improvement in V_{BD} with BT_{donor}. However, V_{BD} achieves a peak value and then starts decreasing, as BT_{donor} is increased further. This V_{BD} roll-off shows a dependence on t_{passi} and t_{ch}. The devices with a thicker t_{ch} or a thicker t_{passi} exhibit V_{BD} roll-off at lower BT_{donor}. Furthermore, an increase in L_{FP} of the device is found to modulate V_{BD} only if device parameters are properly optimized. Fig. 12(b) (inset) shows that such a condition happens only when BT_{donor} is higher (thereby allowing a lateral breakdown), and t_{passi} is optimized to 80 nm for $t_{ch} = 100$ nm. Physical mechanism governing this V_{BD} dependence is discussed in detail in our earlier works [12], [15]. V_{BD} behavior of the device with $t_{passi} = 40$ nm and $L_{FP} = 4\ \mu$m is worth mentioning here. As shown in Fig. 12(b), such devices show a significantly higher V_{BD} and better tolerance to BT_{donor} as compared with other design variants.

2) Minimizing $BT_{acceptor}$: A reduction in $BT_{acceptor}$ is required to improve the dynamic R_{ON} of the device. This is attributed to the fact that the dynamic R_{ON} is caused by electron trapping or hole emission from $BT_{acceptor}$ in the GaN buffer. To find out the possibility of a reduction in $BT_{acceptor}$ without affecting V_{BD} of the device, the following device candidates showing higher V_{BD} were analyzed: 1) devices with $t_{ch} = 100$ and 150 nm for $L_{FP} = 1$ and 4 μm and $t_{passi} \geq 80$ nm and 2) devices with $t_{ch} = 200$ nm for $L_{FP} = 4\ \mu$m and $t_{passi} = 40$ nm. The results for devices with $L_{FP} = 1$ and 4 μm are shown in Fig. 13(a) and (b), respectively. Fig. 13(a) shows that the thinner t_{ch} of 100 nm allows $BT_{acceptor}$ reduction up to 5×10^{17} cm^{-3} irrespective of t_{passi}. On the other hand, a thicker t_{ch} limits the design window with a requirement of a $BT_{acceptor}$ of 7×10^{17} cm^{-3} for $t_{passi} = 80$ nm and 8×10^{17} cm^{-3} for $t_{passi} > 80$ nm. The devices with $L_{FP} = 4\ \mu$m showed a similar dependence for these conditions and, hence, have not been shown here. On the other hand, Fig. 13(b) shows that for $t_{passi} = 40$ nm and $L_{FP} = 4\ \mu$m, the devices allowed reduction in $BT_{acceptor}$ up to 2×10^{17} and 3×10^{17} cm^{-3} for $t_{ch} = 150$ and 200 nm, respectively, without affecting V_{BD}.

B. Buffer Trap Configuration and Dynamic R_{ON}

To analyze the dynamic R_{ON} of the devices optimized for maximum V_{BD}, the device variants allowing $BT_{acceptor} \leq 5 \times 10^{17}$ cm^{-3} are only discussed here. For $BT_{acceptor}$ higher than this, no significant improvement in dynamic R_{ON} was observed. This restricts t_{ch} to 100 nm for $L_{FP} = 1$-μm devices while allowing for an increase in t_{ch} up to 200 nm for $L_{FP} = 4$-μm devices. Fig. 14 compares the dynamic R_{ON} performance of these device variants as a function of $BT_{acceptor}$. Irrespective of device parameters, an improvement in dynamic R_{ON} is observed, as $BT_{acceptor}$ is reduced, as seen in Fig. 14(a)–(e). However, the devices with $L_{FP} = 4\ \mu$m show a lower degree of improvement as compared to devices with $L_{FP} = 1\ \mu$m. This is attributed to the higher magnitude of the electric field near the FP edge for larger L_{FP} devices. This will, in turn, lead to a higher magnitude of charge trapping in the GaN buffer, offsetting any improvement gained by a reduction in $BT_{acceptor}$. However, the use of thinner passivation ($t_{passi} \approx 40$ nm) for devices with larger L_{FP} allows the use of a thicker channel and considerable reduction in $BT_{acceptor}$, as discussed in the previous section. This allows for a significant improvement in the dynamic R_{ON} of these devices, as $BT_{acceptor}$ is lowered, as seen in Fig. 14(d) and (e). A thicker unintentionally doped (UID) GaN channel is desirable for maintaining excellent channel transport properties offered by AlGaN/GaN HEMTs. The above discussion establishes that

a thicker UID GaN channel can be realized by employing a thinner t_{passi} and a larger L_{FP} while simultaneously optimizing C–Si co-doping to minimize dynamic R_{ON} while maximizing V_{BD} of the device.

V. Conclusion

The impact of device design and epi-stack parameters on electron trapping in the GaN buffer and resulting dynamic R_{ON} is disclosed in this work. A higher surface donor trap concentration (ST_{donor}) was found to result in an increased electron injection and trapping in the GaN buffer, resulting in a higher dynamic R_{ON}. This was attributed to an increase in electric field magnitude near the gate and field plate edge due to higher ST_{donor}. The reduction in ST_{donor} required to improve dynamic R_{ON} was found to be correlated with the polarization charge in the AlGaN layer. The polarization charge affected the gate leakage and, hence, modulated electron injection into the GaN buffer and resulting dynamic R_{ON}. Furthermore, the impact of passivation thickness on dynamic R_{ON} of the device was found to be correlated with the GaN channel thickness. This was attributed to the impact of passivation thickness on the electron current leakage path through the GaN buffer. Moreover, the choice of field plate length was also found to affect the interplay between the passivation and the GaN channel thickness in determining the dynamic R_{ON} of the device. Finally, a carbon–silicon co-doping optimization scheme for GaN buffer was discussed in correlation to these parameters while considering its impact on dynamic R_{ON} as well as the breakdown voltage (V_{BD}) of the device. The C–Si co-doping allowed for a reduction in the requirement of C-doping-induced acceptor trap concentration without affecting V_{BD} of the device. This results in an improved dynamic R_{ON} behavior. The devices with thinner channel offered a wider buffer-doping optimization window. However, these devices exhibited a higher dynamic R_{ON} as compared to devices with a thicker channel. On the other hand, V_{BD} of the device reduced significantly with an increase in channel thickness. However, buffer-doping optimization for device variants employing a longer field plate with a thinner passivation dielectric showed the possibility of simultaneously achieving a higher V_{BD} and a lower dynamic R_{ON} even with a thicker channel. The thicker channel helps in maintaining the device's excellent channel transport properties.

References

[1] A. Chini *et al.*, "Experimental and numerical analysis of hole emission process from carbon-related traps in GaN buffer layers," *IEEE Trans. Electron Devices*, vol. 63, no. 9, pp. 3473–3478, Sep. 2016, doi: 10.1109/TED.2016.2593791.

[2] S. D. Gupta, V. Joshi, R. R. Chaudhuri, and M. Shrivastava, "Part I: Physical insights into dynamic R_{ON} behavior and a unique time-dependent critical stress voltage in AlGaN/GaN HEMTs," *IEEE Trans. Electron Devices*, vol. 68, no. 11, pp. 5720–5727, Nov. 2021, doi: 10.1109/TED.2021.3109847.

[3] Y. Saito, R. Tsurumaki, N. Noda, and K. Horio, "Analysis of reduction in lag phenomena and current collapse in field-plate AlGaN/GaN HEMTs with high acceptor density in a buffer layer," *IEEE Trans. Device Mater. Rel.*, vol. 18, no. 1, pp. 46–53, Mar. 2018, doi: 10.1109/TDMR.2017.2779429.

[4] I. Chatterjee *et al.*, "Lateral charge transport in the carbon-doped buffer in AlGaN/GaN-on-Si HEMTs," *IEEE Trans. Electron Devices*, vol. 64, no. 3, pp. 977–983, Mar. 2017, doi: 10.1109/TED.2016.2645279.

[5] M. J. Uren *et al.*, "'Leaky dielectric' model for the suppression of dynamic R_{ON} in carbon-doped AlGaN/GaN HEMTs," *IEEE Trans. Electron Devices*, vol. 64, no. 7, pp. 2826–2834, Jul. 2017, doi: 10.1109/TED.2017.2706090.

[6] A. Koudymov, V. Adivarahan, J. Yang, G. Simin, and M. A. Khan, "Mechanism of current collapse removal in field-plated nitride HFETs," *IEEE Electron Device Lett.*, vol. 26, no. 10, pp. 704–706, Oct. 2005, doi: 10.1109/LED.2005.855409.

[7] H. Yacoub *et al.*, "Effect of carbon doping level on static and dynamic properties of AlGaN/GaN heterostructures grown on silicon," *IEEE Trans. Electron Devices*, vol. 65, no. 8, pp. 3192–3198, Aug. 2018, doi: 10.1109/TED.2018.2850066.

[8] J. Hu, S. Stoffels, S. Lenci, G. Groeseneken, and S. Decoutere, "On the identification of buffer trapping for bias-dependent dynamic R_{ON} of AlGaN/GaN Schottky barrier diode with AlGaN:C back barrier," *IEEE Electron Device Lett.*, vol. 37, no. 3, pp. 310–313, Mar. 2016, doi: 10.1109/LED.2016.2514408.

[9] V. Joshi, S. D. Gupta, R. R. Chaudhuri, and M. Shrivastava, "Physical insights into the impact of surface traps on breakdown characteristics of AlGaN/GaN HEMTs—Part I," *IEEE Trans. Electron Devices*, vol. 68, no. 1, pp. 72–79, Jan. 2021, doi: 10.1109/TED.2020.3034561.

[10] V. Joshi, S. D. Gupta, R. R. Chaudhuri, and M. Shrivastava, "Interplay between surface and buffer traps in governing breakdown characteristics of AlGaN/GaN HEMTs—Part II," *IEEE Trans. Electron Devices*, vol. 68, no. 1, pp. 80–87, Jan. 2021, doi: 10.1109/TED.2020.3034562.

[11] M. J. Anand *et al.*, "Effect of OFF-state stress induced electric field on trapping in AlGaN/GaN high electron mobility transistors on Si (111)," *Appl. Phys. Lett.*, vol. 106, no. 8, 2015, Art. no. 083508, doi: 10.1063/1.4913841.

[12] V. Joshi, S. P. Tiwari, and M. Shrivastava, "Part II: Proposals to independently engineer donor and acceptor trap concentrations in GaN buffer for ultrahigh breakdown AlGaN/GaN HEMTs," *IEEE Trans. Electron Devices*, vol. 66, no. 1, pp. 570–577, Jan. 2019, doi: 10.1109/TED.2018.2878787.

[13] S. D. Gupta, V. Joshi, R. R. Chaudhuri, and M. Shrivastava, "Novel surface passivation scheme by using p-type AlTiO to mitigate dynamic ON resistance behavior in AlGaN/GaN HEMTs—Part II," *IEEE Trans. Electron Devices*, vol. 68, no. 11, pp. 5728–5735, Nov. 2021, doi: 10.1109/TED.2021.3064531.

[14] V. Joshi, A. Soni, S. P. Tiwari, and M. Shrivastava, "A comprehensive computational modeling approach for AlGaN/GaN HEMTs," *IEEE Trans. Nanotechnol.*, vol. 15, no. 6, pp. 947–955, Nov. 2016, doi: 10.1109/TNANO.2016.2615645.

[15] V. Joshi, S. P. Tiwari, and M. Shrivastava, "Part I: Physical insight into carbon-doping-induced delayed avalanche action in GaN buffer in AlGaN/GaN HEMTs," *IEEE Trans. Electron Devices*, vol. 66, no. 1, pp. 561–569, Jan. 2019, doi: 10.1109/TED.2018.2878770.

[16] Z. Tang, S. Huang, Q. Jiang, S. Liu, C. Liu, and K. J. Chen, "High-voltage (600-V) low-leakage low-current-collapse AlGaN/GaN HEMTs with AlN/SiN_X passivation," *IEEE Electron Device Lett.*, vol. 34, no. 3, pp. 366–368, Mar. 2013, doi: 10.1109/LED.2012.2236638.

[17] A. Minetto *et al.*, "Hot-electron effects in AlGaN/GaN HEMTs under semi-ON DC stress," *IEEE Trans. Electron Devices*, vol. 67, no. 11, pp. 4602–4605, Nov. 2020, doi: 10.1109/TED.2020.3025983.